Dynamic ice accretion process and its effects on the aerodynamic drag characteristics of a power transmission cable model

Ramsankar Veerakumar, Linyue Gao, Yang Liu, Hui Hu*

Department of Aerospace Engineering, Iowa State University, Ames, Iowa 50011, USA

A B S T R A C T

An experimental study was conducted to examine the dynamic ice accretion process over the surface of a high-voltage power transmission cable model and characterize the effects of the ice accretion on the aerodynamic forces acting on the test model. The experimental study was carried out by leveraging the unique Icing Research Tunnel of Iowa State University (i.e., ISU-IRT) to generate typical wet glaze and dry rime icing conditions experienced by power transmission cables. A cylindrical power cable model, which has the same diameter as that of typical power transmission cables, was mounted in ISU-IRT for the ice accretion experiments. In addition to using a high-speed digital imaging system to record the dynamic ice accretion process, a novel digital image projection (DIP) based technique was utilized to quantify the 3D shapes of the ice structures accreted on the surface of the power cable model as a function of the ice accretion time. The time variations of the aerodynamic drag force acting on the test model during the dynamic ice accretion process were also measured quantitatively by using high-sensitive force/moment traducers mounted at two ends of the test model. The ice structures accreted over the surface of the power cable model were found to change significantly under different icing conditions (i.e., rime icing vs. glaze icing). The characteristics of the aerodynamic drag acting on the test model was found to vary significantly during the dynamic ice accretion process depending on what types of ice structures were accreted on the test model. The acquired snapshots of the ice accretion images and the measured 3D shapes of the accreted ice structures on the test model are correlated with the aerodynamic force measurement results to elucidate the underlying physics.

1. Introduction

Atmospheric icing on electric power transmission lines/cables has been known to be a serious problem in cold regions. Power cable icing due to freezing rain and/or caused by in cloud icing has been found to reduce the reliability of electrical power distribution networks, leading to major damages to power lines (Gupta et al., 1994; Mulherin, 1998; Wagner, 2008). In extreme cases, ice accretion on power transmission cables/lines has been found to cause severe damages to transmission power cables and associated towers, resulting in extensive electric power breakdown. For instance, a major icing event which occurred in Quebec and Ontario in winter 1998 led to loss of power for about one million customers in the region for about 3–30 days (Farzaneh, 2000). Material damages were also substantial with hundreds of miles of transmission, sub-transmission and distribution lines being destroyed, leading to an estimated cost of one billion of Canadian dollars for re-construction. Social cost involved in the incident was found to exceed three times that amount (Farzaneh, 2008).

The shape and the density of the ice accreted on power cables are of major interest in investigating the potential risks involved. The wide variations of the accreted ice structures in size, density, and shape cause an equally wide variety of loads to be imposed on the structural system of the power transmission lines/cables. The weight of the accreted ice increases the vertical load on the conductors as well as the support structures. Combined effects of ice and wind can cause the transverse loads on a transmission line/cable to increase significantly. It can also cause vibrational loads due to wind if the ice deposition is asymmetric (Pohlman and Landers, 1982). Natural winds can cause wind-induced vibrations (oscillations caused by vortex shedding) on transmission line conductors. These vibrations may adversely affect the reliability and durability of conductors and associated components (Meng et al., 2012). While damping devices may be used to attenuate this, however, when ice precipitations accrete on the conductors, the situation can change dramatically. The vibrations of conductors coated with ice may occur in frequency ranges outside the design range of the dampers. Galloping, another wind-induced instability, would also occur on ice-
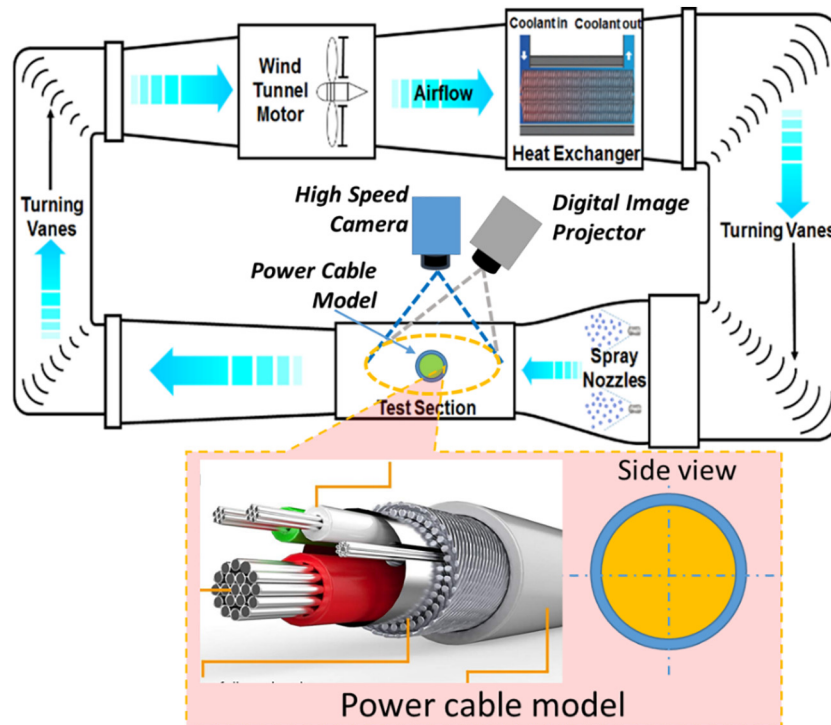

Fig. 1. Schematics of ISU-IRT and the power cable model used in the present study.

accreted conductors and may result in large amplitude low frequency conductor displacements (Farzaneh, 2008) similar to ice coated suspension bridge cables (Górski et al., 2016; Liu et al., 2019). In addition, ice accumulation on power cables may also lead to flashover, where two conductors in wind-induced motion would come in contact and result in electrical discharge across them. Flashover may also happen when ice coated conductor sheds ice which results in sudden vertical displacement of the conductor (Fu et al., 2009; Hrabovský et al., 2017; Ji et al., 2015).

It is well known that, ice accretion on cold surfaces can be of different ice types, depending on the icing conditions. Rime and glaze icing are the two most commonly observed icing conditions – the specific type is dependent on the ambient air temperature, wind velocity, liquid water content (LWC) of the incoming airflow and median volumetric diameters (MVD) of the impinging water droplets. Usually, relatively low temperatures colder than −10 °C and lower LWC level favors a dry regime of icing where all the water impinging on the surfaces immediately freeze to form rime ice. Warmer temperatures around −5 °C and relatively higher LWC level would favor a wet icing regime, where only a portion of the impinging water would freeze in the impingement area and the remaining frozen water runs back and then freezes subsequently in the downstream, causing the formation of glaze ice (Liu et al., 2018; Liu and Hu, 2018). Rime ice accretion usually tends to follow the original contour of the object as the water droplets freeze almost immediately upon impingement on the surface. This is often associated with less aerodynamic penalties. Glaze ice is known as the most dangerous type of ice. As glaze ice is caused by wet icing conditions, it forms much more complicated ice shapes, hence, have much larger detrimental effects on the aerodynamic performance (Gao et al., 2019a; Liu and Hu, 2018).

A better understanding about the dynamic ice accretion process on power transmission cables/lines is highly desirable for the development of counter measures for power cable icing mitigation. While a number of studies has been conducted recently on power cable icing phenomena (Koss et al., 2012; Makkonen, 1998; Makkonen and Wichura, 2010; Qing et al., 2019; Szilder, 2018; Zarnani et al., 2012), very little can be found in literature to quantify the 3D shapes of the ice structures

accreted dynamically on the surfaces of power cables and characterize the time-evolution of aerodynamic forces acting on power cables during the dynamic ice accretion process under different icing conditions. In the present study, a comprehensive experimental investigation was conducted to examine the dynamic ice accretion process over the surface of typical power transmission cables and characterize the effects of the ice accretion on the aerodynamic forces acting on the power cables. The experimental study was conducted in the Icing Research Tunnel available at Iowa State University (i.e., ISU-IRT). A cylindrical power transmission cable model with the same diameter of typical power transmission cables/lines (i.e., $D = 29$ mm) was mounted in ISU-IRT and subjected to both wet glaze and dry rime icing conditions. During the experiments, in addition to using a high-speed imaging system to record the dynamic ice accretion process, a novel digital image projection (DIP) based 3D shape scanning system was also utilized to quantify the 3D shapes of the ice structures accreted on the surface of the power cable model as a function of the ice accretion time. The aerodynamic drag forces acting on the power cable model during the dynamic icing process were also measured by using a pair of high-sensitive force/moment load cell mounted at two ends of the test model. The acquired snapshots of the ice accretion images and the measured 3D shapes of the accreted ice structures on the test model were correlated with the aerodynamic force measurements in order to elucidate the underlying physics for a better understanding of the dynamic ice accretion process and its effects on the aerodynamic characteristics of the power transmission cables/lines.

2. Experimental setup and test model

2.1. Icing research tunnel and test model used in the present study

The experiment study was conducted in the Icing Research Tunnel of Iowa State University (i.e., ISU-IRT). ISU-IRT, which was originally donated by Collins Aerospace System (i.e., formerly Goodrich Corporation), is a newly refurbished research-grade multifunctional icing research tunnel. As shown schematically in Fig. 1, ISU-IRT has a test section of 2.0 m in length × 0.4 m in width × 0.4 m in height with

all of the side walls being optically transparent. It has a capacity of generating a maximum wind speed up to 60 m/s and airflow temperature down to −25 °C. The turbulence level of the oncoming airflow at the entrance of the test section was found to be about 3.0%, as measured by using a hot wire anemometer. A water spray system, which consists of arrays of 8 pneumatic atomizing spray nozzles (Spraying Systems *Co.*, 1/8NPT-SU11), was installed at the entrance of the contraction section of ISU-IRT to inject micro-sized water droplets (10–100 μm in size) into the test section. The desired liquid water content (LWC) level and the medium volumetric diameter (MVD) of the airborne water droplets can be achieved by regulating the water flow rate and air/water pressures supplied to the spray nozzles. In summary, ISU-IRT can be used to simulate atmospheric icing phenomena over a range of icing conditions (i.e., from very dry rime icing to extremely wet glaze icing conditions). By leveraging ISU-IRT, extensive researches have been conducted to study various atmospheric icing phenomena, including aircraft icing, aero-engine icing, wind turbine icing and cable-stayed bridge icing (Gao et al., 2019a; Li et al., 2019; Liu et al., 2019; Liu et al., 2018).

As shown schematically in Fig. 1, a cylindrical test model was mounted horizontally in the test section of ISU-IRT for the present study. The test model was designed to have the same outer diameter as commonly used high-voltage power transmission cables/lines (i.e., $D = 29$ mm), and has the spanwise length of $L = 400$ mm (i.e., the same as the spanwise length of the ISU-IRT test section). The surface of the power cable model used in the present study was found to be hydrophilic with the contact angle of sessile water droplets over the surface of the power cable model being about 65°, which is in the range of the surface wettability of typical power cables as reported in Li et al. (2018).

During the experiments, the velocity of the incoming airflow in ISU-IRT was kept at $V_\infty = 20$ m/s (i.e., a typical wind speed of power cable icing events in cold winters). The corresponding Reynolds number based on the diameter of the test model is about 50,000 (i.e., $Re = 50,000$). Both typical rime and glaze icing conditions that power transmission cables usually experience in cold winters were simulated in the present study. While ambient temperature and the liquid water content (LWC) level of the incoming airflow in ISU-IRT was set at $T_\infty = -5.0$ °C and LWC = 2.0 g/m^3 for the glaze icing experiments, the corresponding testing parameters were set at $T_\infty = -15.0$ °C and LWC = 1.0 g/m^3 for experiments under the rime icing condition.

2.2. Quantification of the dynamic ice accretion process on the surface of the power cable model

In the present study, a high-speed imaging system (PCO-Dimax-S1, acquisition rate up to 25,000 frames per second with 1008 pixels by 1008 pixels in spatial resolution) along with a 60-mm Macro Lens (Nikon, 60 mm Nikkor 2.8D) was used to record the dynamic ice accretion process (i.e., transient water film runback, rivulet formation, and accumulated ice growth) over the ice accreting surfaces of the test model. The camera was positioned vertically above the test model. Low-flicker illumination was provided by a pair of 150 W fiber-coupled halogen lamps (AmScope, HL250-AS). The key features of the dynamic ice accreting process would be revealed qualitatively based on the time sequences of the acquired snapshots of the ice accretion images.

In addition to acquiring snapshot images to visualize the dynamic ice accretion process, a novel digital image projection (DIP) based 3D scanning system was also used to achieve "in-situ" measurements of the 3D shapes of the ice structures with the test model still being mounted inside ISU-IRT. The DIP system is based on the principle of structured light triangulation in a fashion similar to stereo vision technique, but replacing one of the cameras in the stereo pair with a digital projector (Zhang et al., 2015). A digital image with known pattern characteristics was projected onto the test object of interest (i.e., ice structures accreted over the surface of the power cable model for the present study).

Due to the complex three-dimensional (3D) geometrical profiles of the test objects (i.e., the surface of the accreted ice structures), the projected digital patterns are deformed when observed from a perspective different from the projection axis. By comparing the distorted digital patterns (i.e., acquired images with ice structures accreted over the surface of the transmission cable model) with a reference digital pattern without the test objects on the reference surface, the 3D profile of the iced test model can be retrieved quantitatively. Further information about the technical basis and implementation of the DIP system is available in Zhang et al. (2015).

After conducting a careful calibration operation to register the correlation relationship between the digital projector and high-resolution camera, the iced test model was rotated at every 20° around its center for the DIP image acquisitions. The DIP images were processed to retrieve 3D profiles of the ice structures acquired at different phase angles and then combined automatically to reconstruct the 3D shapes of the ice structures accreted over the surfaces of the test model.

It should be noted that, while a number of intrusive techniques have been developed for quantitative measurements of ice shapes accreted over test models, e.g., hand tracing method (Lee et al., 2012), and mold-and-casting method (Blasco et al., 2017), they are usually very time consuming and expensive in implementation (i.e., mold-and-casting method). Furthermore, some of the fragile ice features might even be damaged during the ice shape measurements. More recently, non-intrusive laser light sheet scanning technique has also been developed for 3-D ice shape measurements (Gong and Bansmer, 2015; Woodard et al., 2018). However, the laser scanning method can only measure 2-D profiles of accreted ice structures directly, and relies on a line-by-line scanning operation to reconstruct 3D ice shapes, which could be very time consuming and much involved in instrumentation for high-resolution measurements of complex 3D ice structures. The DIP-based 3D scanning system used in the present study is capable of quantitatively measuring fully 3D shapes of complex ice structures accreted over the power cable model. In comparison with those conventional methods (i.e., hand-tracing method, mold-and-casting method, or laser light sheet scanning technique), the DIP-based 3D scanning system used in the present study is much faster (i.e., ~ 10s for each test case) to achieve full 3D shape measurements of ice structures over the entire span of the test model and also much easier to implement for "in-situ" measurements of 3D ice shapes with the test model still being mounted inside the icing tunnel. For the DIP-based 3D scanning operation, while the airflow was paused, the ambient temperature was kept at the same level as the ice accretion testing. The changes in the morphologies of the ice structures are believed to be very small due to the scanning operation. This technique was used successfully to record the 3D profiles of the ice structures accreted over a wind turbine airfoil at the ISU-IRT (Gao et al., 2019b). While some of the preliminary results of this campaign on transmission cable icing studies were presented in Veerakumar et al. (2019), much more quantitative measurement results and comprehensive analysis/discussions about the experimental observations were given in the present study.

In order to estimate the measurement uncertainty of the DIP-based 3D scanning system, a test plate with a series of roughness elements in the form of hemispheres of different sizes was custom designed and 3D printed with a high-accuracy rapid prototyping machine (i.e., the accuracy level of 10 μm), as shown in Fig. 2(a). Then, the DIP-based 3D scanning system was used to measure the roughness elements 3D printed on the test plate. Since the nominal height distributions of the hemispheres are known, the measurement accuracy of the DIP-based 3D scanning system can be evaluated by quantitatively comparing the measured results against the nominal heights of the hemispheres. Fig. 2(b) gives the quantitative comparison of the measured profiles against the nominal data of both the concave and convex hemispheres of 8.0 mm in diameter along two arbitrarily selected traces passing through the centers of the hemispheres. It can be seen clearly that the measured results agree with the nominal height profiles very well for
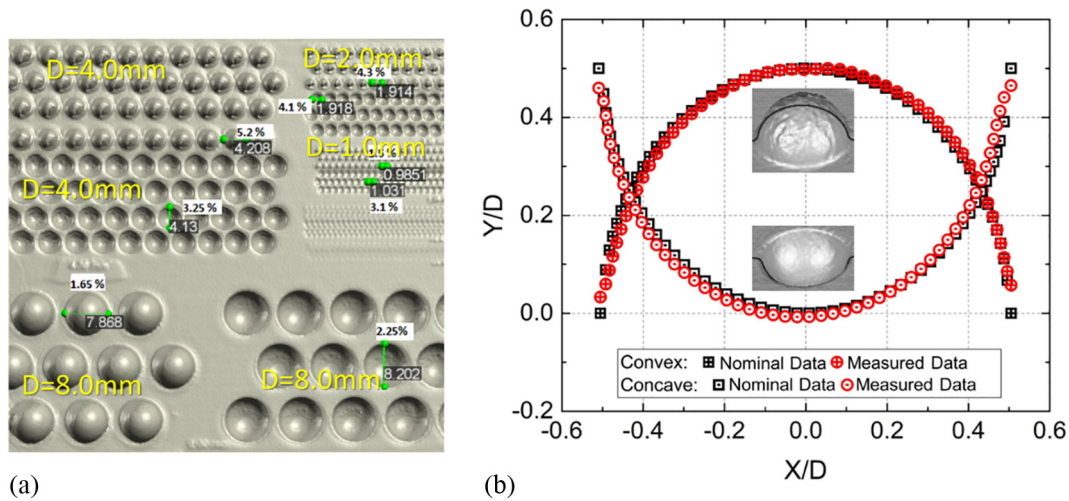
Fig. 2. The test plate and the measured profiles by using the DIP-based 3-D scanning system.
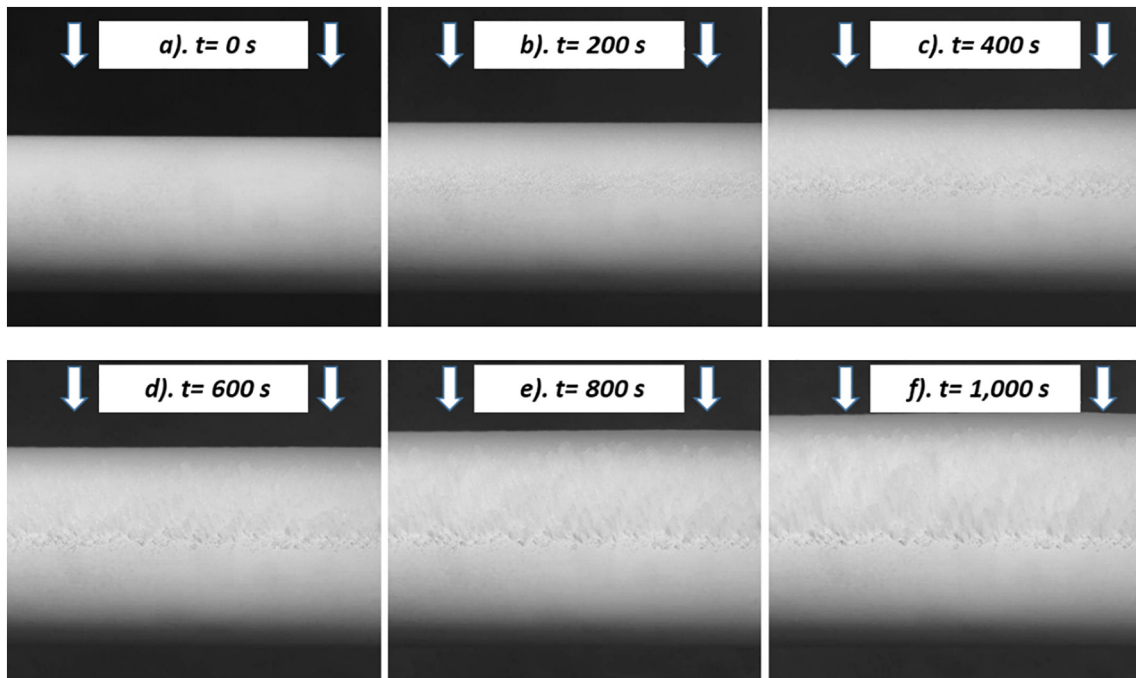

Fig. 3. Typical snapshots of the ice structures accreted over the surface of the test model under a typical rime icing condition of $V_\infty = 20$ m/s, $T_\infty = -15\,°$C, and LWC = 1.0 g/ m^3.

both the concave and convex hemispheres. Based on the measurement data at about 500 points around the hemispheres, the mean and root-mean-squared (i.e., RMS) values of the differences between the measurement results and the nominal values were calculated. The averaged difference between the measurement results and the nominal height values (i.e., the measurement uncertainty of the DIP-based 3D scanning system) was found to be ~150 μm, which is about 2.0% of the nominal diameters of the 8.0 mm hemispheres. Similar measurement uncertainty level was also found for the other hemispheres with different diameters.

2.3. Aerodynamic force measurements with high-sensitive, multi-axis force-moment transducers

In the present study, a pair of high-sensitive, multi-axis force-moment transducers (ATI-IA Mini 45) were mounted at two ends of the power cable model to measure the unsteady aerodynamic forces acting on the test model during the dynamic ice accreting process. The force/moment transducers are composed of foil strain gage bridges, which can measure the aerodynamic forces along three orthogonal axes, and the moment (torque) about each axis. The precision of the force-moment transducer for the force measurements is ± 0.25% of the full range (10 N). During the experiments, the two sets of the force/torque transducers were synchronized via a 16-bit data acquisition system (NI USB-6218) at a data acquisition frequency of 1000 Hz. More details of the force transducer and the force measuring technique could be found in the recent work of Gao et al. (2019a, 2019b).

3. Experimental results and discussion

Before performing the ice accretion experiments, ISU-IRT was operated at a pre-scribed frozen-cold temperature level (i.e., −15.0 °C for the rime icing experiments and − 5.0 °C for the glaze icing experiment for the present study) for at least 20 min to ensure ISU-IRT reaching a

thermal steady state. Since the temperature inside the ISU-IRT was set to be well below the freezing temperature of water (i.e. 0.0 °C), after switching on the water spray system of the ISU-IRT, the water droplets exhausted from the water spray nozzles would be in a super-cooled state. Dynamic ice accretion process was found to start immediately, upon the impact of the super-cooled water droplets onto the power cable model.

3.1. The experimental results under the rime icing condition

As described above, the ice accretion process over a solid surface can be either glaze icing and rime icing process, depending on the combined effects of ambient temperature, wind speed, size of the super-cooled water droplets, and Liquid Water Content (LWC) level in the incoming airflow (Anderson and Tsao, 2005; Liu and Hu, 2018). Fig. 3 shows typical snapshot images of the ice accretion process to reveal the dynamic ice accretion process over the surface of the test model under a typical rime icing condition of $V_\infty = 20$ m/s, $T_\infty = -15$ °C, and LWC = 1.0 g/ m³. The snapshot images were acquired at six representative instants (i.e., of 0 s, 200 s, 400 s, 600 s, 800 s and 1000 s) after switching on the water spray system. It can be seen clearly that, since the icing experiment was conducted under a very cold condition (i.e., $T_\infty = -15$ °C), the super-cooled water droplets were found to be frozen into ice almost instantly upon impacting onto the surface of the power cable model. As described in Liu and Hu (2018), since the latent heat of fusion released during the phase changing process of the impinged super-cooled water droplets would be removed/dissipated very rapidly under the rime icing condition, all the impacted water droplets were found to be frozen into solid ice immediately. The ice structures were found to accumulate mainly around the leading edges of the power cable model (i.e., mainly within the direct impinging zone of the super-cooled water droplets) without any noticeable surface water runback on the surface of the test model. The accreted ice structures were found to be rather rough, and have milk-white and opaque appearances. Such experimental observations are found to be of the typical characteristics of a rime icing process, as described in Liu and Hu (2018). As the ice accretion time increases, while the ice layer accreted on the front surface of the power cable model were found to become thicker and thicker, the outer profile of the iced test model was found to become rougher and rougher.

Fig. 4 gives the typical measurement results of the DIP-based 3D scanning system at six representative instants after starting the ice accretion experiment. The characteristics of the dynamic ice accreting process as well as time evolution of the complex ice structures accreted

over the surface of the power cable model were revealed much more clearly and quantitatively. Based on the measured 3D shapes of the ice structures accreted over the surface of the test model, the outer profiles of the ice layer accreted on the power cable model can be extracted. Fig. 5(a) gives of the outer profiles of the ice layer accreted on the test model as a function of the ice accretion time by extracting the 3D shapes of the ice structures accreted at the middle section of the test model. Fig. 5(b) shows the extracted profiles of the ice layer accreted on the test model at five selected sections at different spanwise locations after performing 1000 s of the ice accretion experiment.

Based on the quantitative measurements of the ice structures accreted over the surface of the power cable model as those shown in Figs. 4 and 5, the characteristics of the dynamic ice accretion process were shown more clearly and quantitatively. As described above, upon impact of the super-cooled water droplets onto the surface of the test model, a layer of ice was found to form immediately over the surface of the power cable model, mainly on the front surface. As shown quantitatively in Fig. 5, the rime ice accretion was found to be restricted within the direct impinging zone of the super-cooled water droplets with the upper and lower limits of the rime ice layer accreted on the test model at $\theta_{upper\text{-}limit} \approx 75^0$ and $\theta_{lower\text{-}limit} \approx -75^0$, respectively. Since the impacted super-cooled water droplets would be frozen into solid ice instantly under the rime icing condition, no runback water and/or formation of runback ice on the backside of the test model was observed. It can also be seen that, corresponding to the continuous impact of more and more super-cooled water droplets onto the test model, while the thickness of the ice layer accreted on front surface of the test model increases monotonically, the surface of the iced power cable model was found to become rougher and rougher, as the ice accretion time increases.

As described in Anderson and Tsao (2005), the rime ice accretion process would be affected mainly by the distribution characteristics of the collection efficiency of the super-cooled water droplets carried by the incoming airflow. Corresponding to the higher water collection efficiency in the region near the leading edge of the test model (Pourbagian and Habashi, 2013), the thickness of the ice layer accreted near the leading edge of the power cable model was found to increase much faster than those at further downstream regions, as shown clearly in Fig. 5(a). As a result, the shape of the iced test model was found to be elongated more significantly along the airflow direction, which makes the outer profile of the iced test model to become more and more "streamlined" in shape, instead of the original circular shape (i.e., a bluff body), as the ice accretion time increases. The obvious shape change of the test model due to the ice accretion would cause
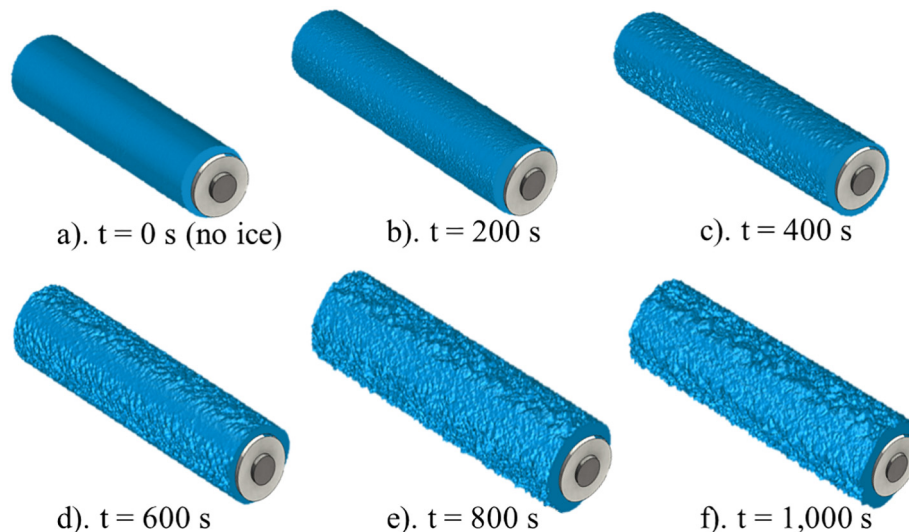

a). t = 0 s (no ice)   b). t = 200 s   c). t = 400 s

d). t = 600 s   e). t = 800 s   f). t = 1,000 s

Fig. 4. Measured 3D shapes of the ice structures accreted on the surface of the test model under the rime icing condition.
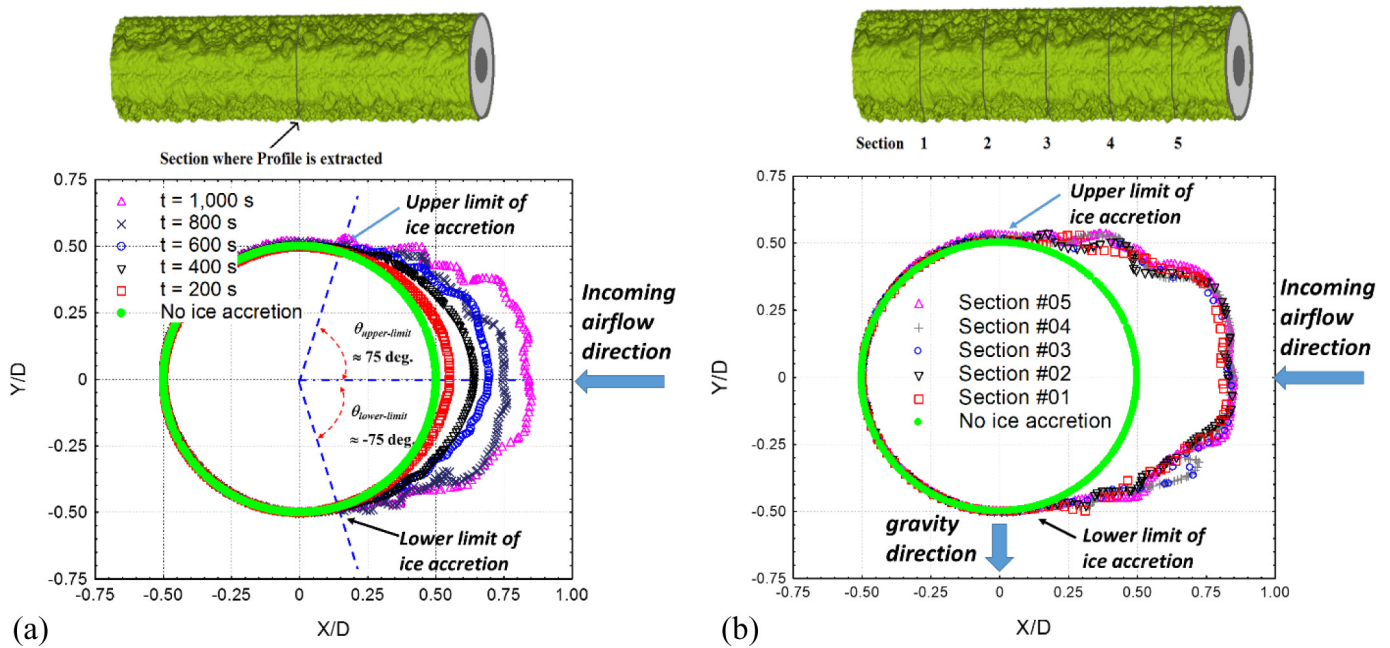
Fig. 5. Extracted profiles of the ice layer accreted on the test model under the rime icing condition.

significant changes on the aerodynamic forces acting on the test model, which was shown quantitatively from the aerodynamic force measurements to be described later.

As indicated schematically in Fig. 5, while the ice accretion experiment of the present study was conducted with the direction of the gravity force being normal to the incoming airflow direction, the ice structures accreted over the surface of the test model were found to be almost symmetric in relation to the incoming airflow direction under the rime icing condition. It indicates that the gravity force would not affect the rime ice accretion process over the test model, since the impacted super-cooled water droplets would be frozen into solid ice instantly upon impacting onto the test model. As shown quantitatively in Fig. 5(b), the outer profiles of the ice layer extracted at different spanwise sections were found to agree with each other well, indicating that the ice structures accreted on the power cable model would be rather uniform along the spanwise direction of the test model under the rime icing condition.

As described above, the aerodynamic forces acting on the power cable model during the dynamic ice accreting process were also measured by using a pair of high-sensitive force-moment transducers (ATI-IA Mini 45) mounted at two ends of the test model. Fig. 6 gives the measured aerodynamic drag data as a function of ice accretion time
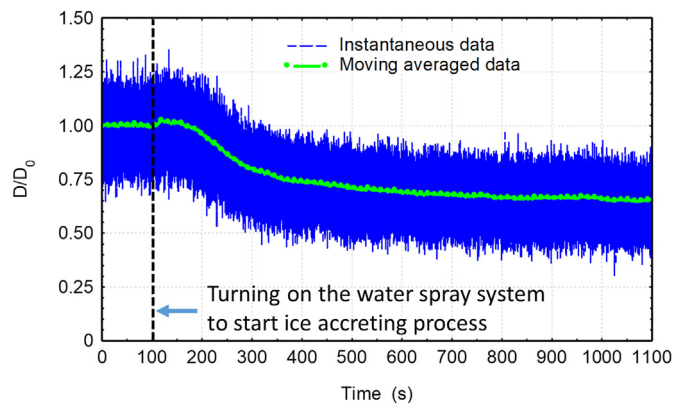

Fig. 6. The measured aerodynamic drag acting on the test model under the rime icing condition.

under the rime icing condition. While the total duration of the force measurements was 1100 s, the water spray system of ISU-IRT was switched on at 100 s after turning on the force-moment transducers (i.e., to start the ice accretion process at $t = 100$ s). By averaging the measured measurement data within the first 100 s (i.e., before starting the ice accretion process), the mean value of the aerodynamic drag acting on the test model, D_0, was calculated. In the present study, the value of D_0 is used as the baseline to evaluate the effects of the dynamic ice accretion process on the aerodynamic drag forces acting on the power cable model. It should be noted that, the corresponding drag coefficient of the power cable model for the test case without any ice accretion was found to be 1.16 (i.e., $C_D = 1.16$). The measurement result of the present study was found to be in good agreement with the standard drag coefficient value (i.e., $C_D = 1.20$) of a circular cylinder reported in the previous studies at the same Reynolds number level (Schlichting et al., 2000).

It should be noted that, the projected area of the iced test model along the airflow direction would change dynamically due to the ice accumulation over the test model during the ice accretion experiment. Instead of using drag coefficient, the aerodynamic drag data measured during the dynamic ice accretion process were presented in term of normalized drag force, i.e., the measured instantaneous drag data were normalized by the baseline drag D_0. Hence, the label of Y-axis in Fig. 6 is set as D/D_0. As described above, while the instantaneous drag acting on the test model were acquired with a data acquisition frequency of 1000 Hz, the moving averaged values of the instantaneously measured drag data (i.e., averaging over every 5 s of the instantaneous measurements) were also calculated and plotted in Fig. 6 for comparison.

It can be seen clearly that, induced by the periodic shedding of the unsteady vortices from two sides of the cylindrical test model similar as those described in Chen et al. (2014), the instantaneous aerodynamic forces acting on the power cable model were found to fluctuate significantly. After the water spray system was switched on at $t = 100$ s, the super-cooled water droplets would impinge onto the surface of the test model to start the ice accretion process immediately, mainly on the front surface of the test model (i.e., within the direct impinging zone of the super-cooled droplets) as shown clearly in Fig. 5. The formation of the rime ice structures at the initial stage of the icing process (i.e., $t = 100$ s ~ 150 s) would result in a much roughened surface of the test model. This would affect the development of the boundary layer airflow

(i.e., laminar boundary layer growth, transition and separation) over the front surface of the test model greatly. The much roughed surface near the leading edge of the power cable model due to the rime ice accretion would result in a greater friction force, thereby, causing the slight increase of the drag force (i.e., ~4% greater) at the initial stage of the rime icing process (i.e., $t = 100\,s \sim 150\,s$), as shown clearly in Fig. 6.

As the time increases, with more and more super-cooled water droplets impinging onto the test model, the ice layer accreted over the front surface of the power cable model would become thicker and thicker, which would change the outer profile of the iced test model substantially. As shown clearly in Fig. 5, the rime ice accumulation on the front surface of the test model tends to make the outer profile of the iced power cable model to change gradually from a cylindrical-shaped bluff body to a "streamlined" body. As a result, the aerodynamic drag force acting on the ice accreting test model was found to decrease gradually as the ice accretion time increases. More specifically, due to the substantial rime ice accretion on power cable model, the averaged aerodynamic drag force acting on the test model at $t = 1100\,s$ (i.e., after 1000 s of the ice accretion experiment) was found to become only about 65% of the baseline value (i.e., the value without any ice accretion on the test model).

3.2. The experimental results under a typical glaze icing condition

In the present study, the dynamic ice accretion process and its combined effects with the wind loads acting on the power cable model were also investigated under a typical glaze icing condition. For the glaze icing experiments, while the velocity of the incoming airflow in ISU-IRT was still kept at $V_\infty = 20\,m/s$, the ambient temperature was increased to a much warmer level (i.e., $T_\infty = -5\,°C$) and the LWC level in the incoming airflow was also much higher (i.e., LWC $= 2.0\,g/m^3$). Fig. 7 shows the typical snapshot images to reveal the dynamic ice accretion process over the surface of the power cable model under the glaze icing condition. It can be seen clearly that, the glassy ice structures accreted over the surface of the test model was found to be transparent, and have a smooth-looking appearance with obvious water

runback under the glaze icing condition, which are the typical features of a glaze icing process as described by Liu et al. (2015). The experimental observation can be explained by the fact that, corresponding to the much higher LWC level in the incoming airflow under the glaze icing condition, much more super-cooled water droplets would impact onto the surface of the test model and undergo phase changing (i.e., solidification) process within the same time duration. Thus, a much more significant amount of latent heat of fusion would be released over the surface of the test model within the same duration of the ice accretion experiment. Due to the higher ambient temperature (i.e., $T_\infty = -5\,°C$) under the glaze icing condition, the significant amount of the latent heat of fusion released during the solidification process could not be removed/dissipated fast enough by convective and/or conductive heat transfer process. This would result in the local accumulation of the released latent heat of fusion over the icing accreting surface of the test model. Therefore, only a portion of the super-cooled water droplets were found to be frozen into solid ice upon impact, while rest of the impinged water mass would still stay in liquid state. Driven by the airflow around the test model, the unfrozen water mass was found to run back over the ice accreting surface of the test model to form rivulet flows, similar as those described by Zhang et al. (2015). The runback surface water was found to be frozen into solid ice subsequently to form rivulet-shaped ice structures at further downstream locations (i.e., in the downstream region beyond the direct impinging zone of the super-cooled droplets). As the time increases, with more and more super-cooled water droplets impacting onto the test model, the ice layer accreted on the power cable model was found to become thicker and thicker, as shown clearly in Fig. 7.

The characteristics of the dynamic ice accretion process under the glaze icing condition were shown much more clearly and quantitatively from the measured 3D shapes of the ice structures accreted over the surface of the power cable model. While Fig. 8 shows the time evolution of the 3D-shapes of the glaze ice structures accreted over the surface of the test model measured by using the DIP-based 3D scanning system, Fig. 9 gives the outer profiles of the accreted glaze ice layer extracted from the measurement results of the 3D scanning system. As described above, under the glaze icing condition, since not all of the super-cooled
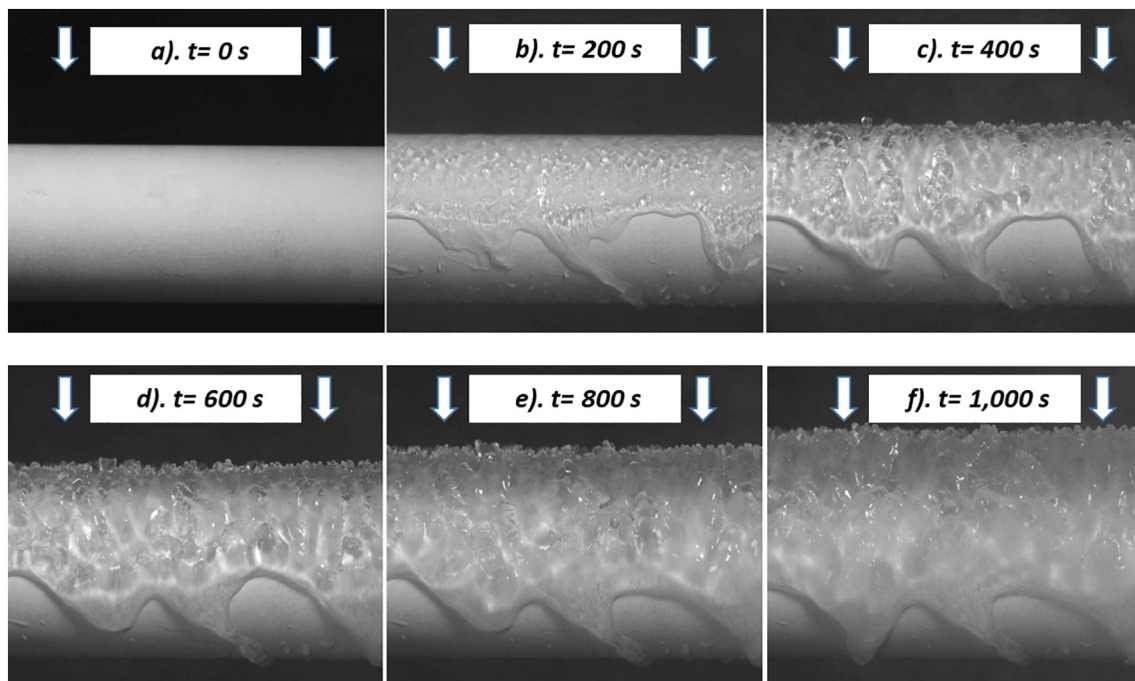

Fig. 7. Typical snapshots of the ice structures accreted over the surface of the test model under a typical glaze icing condition of $V_\infty = 20\,m/s$, $T_\infty = -5\,°C$, and LWC $= 2.0\,g/m^3$.
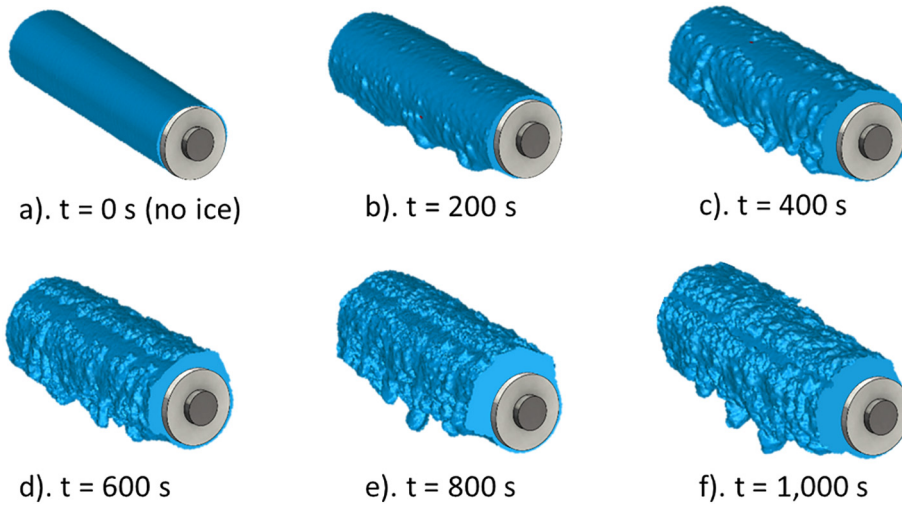
Fig. 8. 3D shapes of the ice structures accreted on the test model under the glaze icing condition.

water droplets would be frozen into solid ice instantly after impinging onto the test model, a portion of the impacted water mass would stay in liquid over the surface of the test model. Driven by the airflow around the test model, the unfrozen water would run back, and re-distribute the impacted water mass over the ice accreting surface of the test model. Therefore, as shown clearly in Fig. 9(a), the glaze ice layer accreted over the surface of the test model was found to be much more uniformly distributed along the azimuthal direction. In comparison, the accreted ice layer would grow much faster in the region near the leading edge of the test model under the rime icing condition. As a result, the outer profile of the iced test model was found to stay as a cylindrical-shape buff-body under the glaze icing condition, instead of becoming "streamlined-shape" due to the ice accretion as that under the rime icing condition. It can also be seen that, as the time increases, while the accreted ice layer over the surface of the test model was found to become thicker and thicker, the iced test model was found to stay as

a bluff body in general with the diameter of the cylindrical-shaped ice layer becoming bigger and bigger.

It can be seen that, as driven by the frozen-cold airflow around the test model, the unfrozen surface water was found to run back rapidly to form rivulet flows over the ice accreting surface, causing the formation of complex rivulet-shaped ice structures over the surface of the model. As shown clearly in Fig. 9(b), due to the formation of the isolated, rivulet-shaped ice structures over the surface of the test model, the thickness of the ice layer accreted over the test model was found to vary significantly along the spanwise direction of the test model.

As described and shown clearly in Fig. 5, since the rime icing process would be restricted within the direct impinging zone of the super-cooled water droplets, the upper and lower limits of the rime ice layer accreted on the front surface of the test model were found to be at $\theta_{upper\text{-}limit} \approx 75^0$ and $\theta_{lower\text{-}limit} \approx -75^0$, respectively. However, under the glaze icing condition, since the water runback would transport the
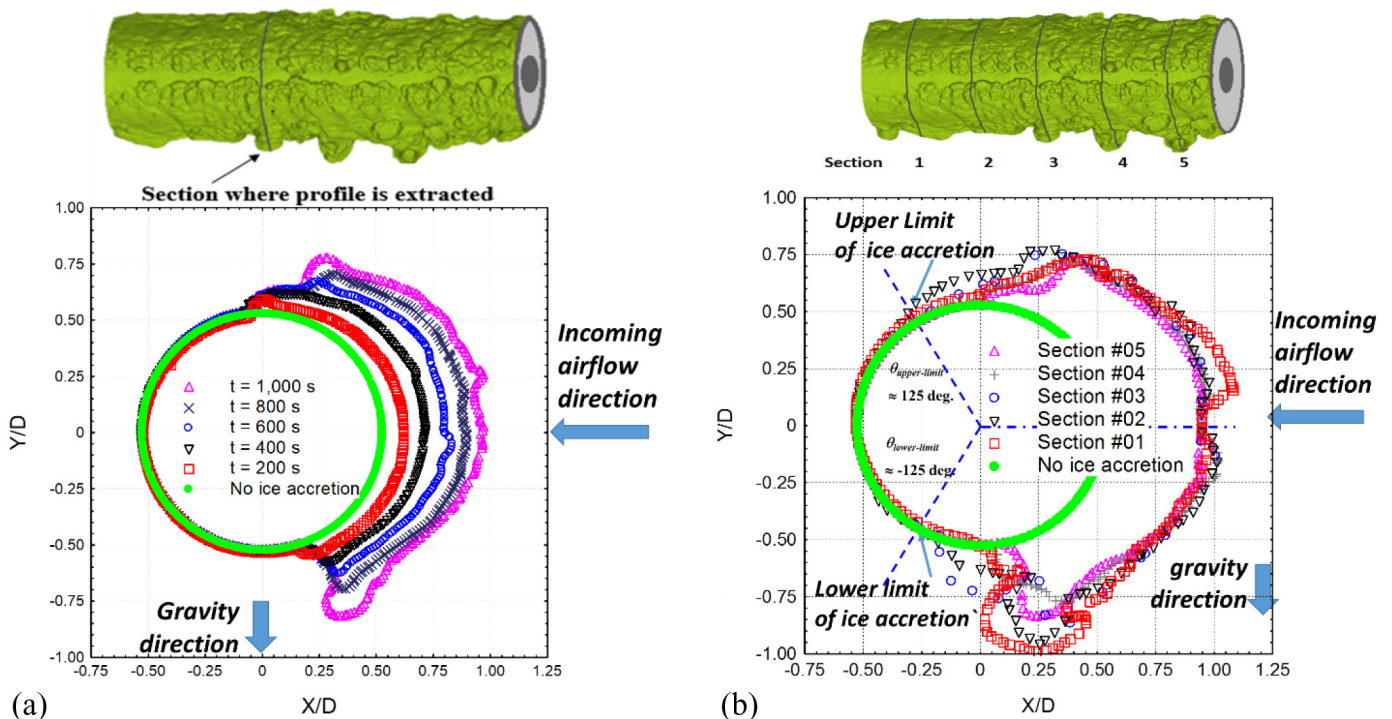

Fig. 9. Extracted profiles of the ice layer accreted on the test model under the glaze icing condition.
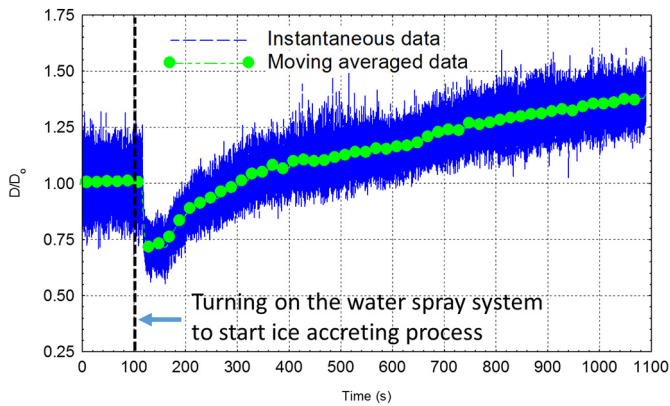
Fig. 10. Measured aerodynamic drag force acting on the test model under the glaze icing condition.

unfrozen water mass to much further downstream regions (i.e., beyond the direct impinging zone of the super-cooled water droplets), the glaze ice layer accreted on the surface of the test model was found to have a much wider coverage. As shown clearly in Fig. 9(b), the upper and lower limits of the glaze ice layer accreted over the test model were found to reach to $\theta_{upper-limit} \approx 125^0$ and $\theta_{lower-limit} \approx -125^0$, respectively.

It can also be seen that, due to the gravity effect, the runback water over the lower surface of the test model was found to more readily to break into rivulet flows, and then form more complicated runback ice structures subsequently near the bottom of the test model, in comparison to those over the upper surface of the test model. Since the irregular-shaped runback ice structures accreted over the surface of the test model would intrude further into the incoming airflow to cause large-scale flow separation, it would induce much greater aerodynamic drag force acting on the iced test model, which was revealed more quantitatively from the force measurements given in Fig. 10.

As shown clearly Fig. 10, the characteristics of the dynamic aerodynamic drag force acting on the power cable model under the glaze icing condition were found to be quite different from those under the rime icing condition. As described above, since the impacted super-cooled water droplets could not be frozen into solid ice completely under the glaze icing condition, the unfrozen water mass would run back over the surface of the test model, driven by the airflow around the test model. At the initial stage of the glaze icing process (i.e., within the first 20 s of the ice accretion process), while the ice layer accreted on the test model is still very thin, the existence of the runback water film would affect the development of the boundary layer airflow over the front surface of the test model greatly. More specifically, in comparison to the "dry" surface case (i.e., without runback water on the test model), the runback water film over the front surface of the test model could act as a "lubricant" to make the airflow moving more smoothly around the "wet" surface of the test model. It would make the "wet" surface of the test model becoming a "slip" surface for the boundary layer airflow over the test model. This would delay the separation of the boundary layer air stream flowing over the surface of the test model. As a result, the aerodynamic drag force acting on the power cable model was found to decrease greatly at the initial stage of the glaze ice accretion process (i.e., up to 25% drag reduction within ~ 20 s after turning on the water spray system of ISU-IRT) as shown clearly in Fig. 10.

As the ice accretion time increases, with more and more super-cooled water droplets impinging onto the test model, the glaze ice layer accreted over the surface of the test model would become thicker and thicker. Due to the continuously increasing diameter of the iced test model as shown quantitatively in Fig. 9(a), the projected area of the iced power cable model along the incoming airflow direction would become bigger and bigger. As a result, the aerodynamic drag force

acting on the test model was found to increase monotonically as the ice accretion time increases. Furthermore, as shown clearly in Figs. 8 and 9, more and more irregular-shaped runback ice structures were found to form over the surface of the test model due to the subsequent freezing of the runback water at the later stage of the glaze icing process (i.e., after 200 s of the ice accretion experiment). The formation of the irregular-shaped runback ice structures would induce large-scale flow separation, which would also contribute to the continuous increase of the aerodynamic drag force acting on the iced power cable model under the glaze icing condition.

3.3. Growth of the ice mass accumulated on the test model under the rime and glaze icing conditions

Based on the measurement results of the DIP-based 3D scanning system as those shown in Figs. 4 and 8, the total volume of the ice structures accreted on the power cable model under both the rime and glaze icing conditions can also be determined. As reported in the recent study of Liu et al. (2017), while the density of typical glaze ice is about 900 kg/m³, the density of typical rime ice would be about 880 kg/m³. Therefore, the total mass of the ice structures accreted over the surface of the power cable model as a function of the ice accretion time under both the rime and glaze icing conditions can also be determined quantitatively.

Fig. 11 gives the measured ice mass accumulation on the power cable model within a unit span as a function of the ice accretion time. It can be seen clearly that, the ice mass accumulated on the power cable model was found to increase monotonically with the increasing ice accretion time under both the rime and glaze icing conditions, as expected. However, the growth characteristics of the ice mass accumulated on the test model were found to be quite different under different icing conditions. While the mass of the ice layer accumulated on the test model would increase linearly with the ice accretion time under the rime icing condition, the ice mass accumulated on the test model was found to grow much faster under the glaze icing condition with its relationship to the ice accretion time being fitted well by using a parabolic function. More specifically, while the LWC level of the incoming airflow for the rime icing experiments was set at LWC = 1.0 g/m³ in the present study, the LWC level for the glaze icing case was at LWC = 2.0 g/m³, (i.e., 2 times of that of the rime icing case). However, after the same ice accretion duration of 1000 s, while the mass of the ice layer accumulated on the power cable model under the rime icing condition was found to be about 0.209 kg/m, the corresponding value under the glaze icing condition was found to become 0.598 kg/m (i.e., about 3 times as that of the rime icing case). The significant difference in the growth of the ice mass accumulated on the test model is believed to be closely related to the different characteristics of the dynamic ice
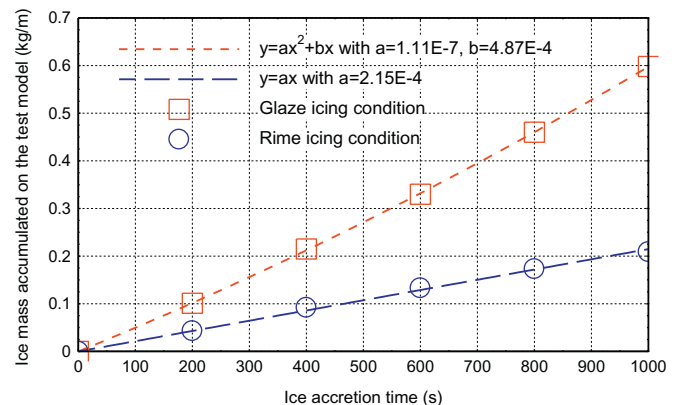

Fig. 11. Measured ice mass accumulated on the test model as a function of the time.

accretion process under the rime and glaze icing conditions.

As described above, the ice structures would accrete only on the front surface of the power cable model (i.e., only within the direct impinging zone of the super-cooled water droplets) under the rime icing condition. As the ice accretion time increases, while the rime ice layer accreted over the front surface of the test model would become thicker and thicker, the outer profile of the iced test model was found to become more and more in "streamlined" shape. As shown quantitatively in Fig. 5, the projected area of the iced test model along the incoming airflow direction (i.e., the area to catch the super-cooled water droplets carried by the incoming airflow) was found to be almost unchanged during the entire duration of the ice accretion experiment. Therefore, the mass of the ice layer accumulated on the power cable model was found to increase linearly with the ice accretion time under the rime icing condition, as shown clearly in Fig. 11.

In comparison to the scenario of the rime ice accretion process, the dynamic icing process under glaze icing condition was found to become much more complicated, due to the existence of the unfrozen water mass that can run back readily over the ice accreting surface of the test model. As described above, under the glaze icing condition, since the runback of the unfrozen water would re-distribute the impacted water mass over the surface of the test model, the glaze ice layer accumulated on the test model was found to have a much wider coverage and become more uniformly distributed azimuthally. The outer profile of the iced test model was found to be still in cylindrical-shape, as shown clearly in Fig. 9. As the ice accretion time increases, with the glaze ice layer accreted over the surface of the test model becoming thicker and thicker, the outer dimeter of the iced test model was found to become bigger and bigger. As a result, the projected area of the iced test model along the incoming airflow direction was found to increase continuously with the ice accretion time. Correspondingly, the airborne super-cooled water droplets over a much wider range would impact onto the iced test model and turn into solid ice, resulting in the much rapid, nonlinear growth of the ice mass accumulated on the test model. Furthermore, as shown clearly in Figs. 8 and 9, more and more irregular-shaped ice structures would be formed on the test model at the later stages of the glaze icing process, due to the frozen of the runback water to form rivulet-shaped ice structures. The irregular-shaped runback ice structures would protrude further into the incoming airflow, thereby, catch more airborne super-cooled water droplets to further promote the rapid growth of the ice mass accumulated on the power cable model at the later stages of the glaze icing process.

4. Conclusions

In the present study, an experimental investigation was conducted to examine the dynamic ice accretion process over the surfaces of typical high-voltage power transmission cables and characterize the effects of the ice accretion on the aerodynamic forces acting on the power cables. The experimental study was performed by leveraging an Icing Research Tunnel available at Iowa State University (i.e., ISU-IRT) to generate typical atmospheric icing conditions (i.e., both wet glaze and dry rime icing conditions) experienced by power transmission cables. A cylindrical test model, which has the same diameter as that of typical power transmission cables (i.e., $D = 29\,mm$), was mounted in ISU-IRT for the ice accretion experiments. In the present study, the velocity of the incoming airflow in ISU-IRT was kept at a constant value of $V_\infty = 20\,m/s$ during the ice accretion experiments. While the temperature and the liquid water content (LWC) level of the incoming airflow was set to be at $T_\infty = -5.0\,°C$ and $LWC = 2.0\,g/m^3$ for the glaze icing experiments, the corresponding values were set to be $T_\infty = -15.0\,°C$ and $LWC = 1.0\,g/m^3$ for the experiments under the rime icing condition. In addition to using a high-speed digital imaging system to record the dynamic ice accretion process, a novel digital image projection (DIP) based 3D scanning system was also used to quantify the 3D shapes of the ice structures accreted on the surface of

the power cable model as a function of the ice accretion time. The time variations of the aerodynamic drag forces acting on the test model during the dynamic ice accretion process were also measured quantitatively by using a pair of high-sensitive force/moment traducers mounted at two ends of the test model.

It was found that, after impacting onto the surface of the power cable model, the super-cooled water droplets carried by the incoming airflow would be frozen into solid ice instantly under the rime icing condition. While the ice structures were found to accrete mainly within a relatively narrow region on the front surface of the test model (i.e., within the direct impinging zone of the super-cooled water droplets), the outer profile of the iced power cable model was found to become more and more streamlined in shape. While the rime ice structures accreted on the surface of the test model were found to be opaque and have a rough, milk-white appearance, the total mass of the ice layer accumulated on the test model was found to increase linearly with the ice accretion time.

The dynamic ice accretion process over the surface of the test model was found to become much more complicated under the glaze icing condition. Upon impacting onto the surface of the test model, only a portion of the super-cooled water droplets would be frozen into solid ice instantly, and the rest of the impacted water mass would stay in liquid state. The unfrozen surface water was found to run back freely, driven by the airflow around the test model. Since the water runback would re-distribute the impacted water mass, the glaze ice layer accumulated on surface of the power cable model was found to have a much wider coverage and become more uniformly distributed azimuthally. As the ice accretion time increases, while the glaze ice layer accreted over the surface of the test model was found to become thicker and thicker, the outer profile of the iced test model was found to be still in cylindrical shape. With the continuous increase of the outer diameter of the iced test model, the airborne super-cooled water droplets over a much greater region would be able to impinge onto the iced test model and turn into solid ice subsequently. As a result, the total mass of the glaze ice accumulated on the test model was found to grow much faster with a nonlinear relationship to the ice accretion time.

The characteristics of the aerodynamic drag force acting on the power cable model was found to be highly dependent on the type of ice structures that accreted on the test model. Under the rime icing condition, while the aerodynamic drag force acting on the power cable model was found to increase slightly (i.e., $\sim 4\%$ increase) at the initial stage of the rime icing process, then decrease gradually as the ice accretion time increases. Since the rime ice accretion would make the iced test model to be more and more streamlined in shape, the aerodynamic drag force acting on the iced test model was found to reduce to only $\sim 65\%$ of the baseline case (i.e., the case without any ice accretion on the test model) after 1000 s of the ice accretion experiment. On the contrary, the aerodynamic drag acting on the test model was found to decrease substantially (i.e., up to 30% in drag reduction) at the early stage of the glaze icing process, then increase monotonically with the ice accretion time under the glaze icing condition. After the same ice accretion time of 1000 s, the aerodynamic drag force acting on the iced test model after 1000 s of the glaze ice accretion experiment was found to increase to $\sim 140\%$ of the baseline case.

References

Anderson, D.N., Tsao, J.-C., 2005. Overview of Icing Physics Relevant to Scaling. NASA/CR—2005-213851. https://doi.org/10.4271/2003-01-2130.

Blasco, P., Palacios, J., Schmitz, S., 2017. Effect of icing roughness on wind turbine power production. Wind Energy 20, 601–617. https://doi.org/10.1002/we.2026.

Chen, W.-L., Li, H., Hu, H., 2014. An experimental study on a suction flow control method to reduce the unsteadiness of the wind loads acting on a circular cylinder. Exp. Fluids 55, 1707. https://doi.org/10.1007/s00348-014-1707-7.

Farzaneh, M., 2000. Ice accretions on high-voltage conductors and insulators and related phenomena. Philos. Trans. R. Soc. A Math. Phys. Eng. Sci. 358, 2971–3005. https://doi.org/10.1098/rsta.2000.0692.

Atmospheric icing of power networks. In: Farzaneh, M. (Ed.), Antiicing and De-icing Techniques for Overhead Lines, 2008th ed. vol. 2008 Springer Science & Business Media Chap. 6.

Fu, G., Wang, L., Guan, Z., Meng, X., 2009. Study on the prevention of conductor ice-shedding by interphase spacer. In: Proceedings of the IEEE International Conference on Properties and Applications of Dielectric Materials. IEEE, pp. 49–52. https://doi.org/10.1109/ICPADM.2009.5252510.

Gao, L., Liu, Y., Zhou, W., Hu, H., 2019a. An experimental study on the aerodynamic performance degradation of a wind turbine blade model induced by ice accretion process. Renew. Energy 133, 663–675. https://doi.org/10.1016/J.RENENE.2018.10.032.

Gao, L., Veerakumar, R., Liu, Y., Hu, H., 2019b. Quantification of the 3D shapes of the ice structures accreted on a wind turbine airfoil model. J. Vis. 22, 661–667. https://doi.org/10.1007/s12650-019-00567-4.

Gong, J., Bansmer, S., 2015. Laser scanning applied for ice shape measurements. Cold Reg. Sci. Technol. 115, 64–76. https://doi.org/10.1016/j.coldregions.2015.03.010.

Górski, P., Pospíšil, S., Kuznetsov, S., Tatara, M., Marušić, A., 2016. Strouhal number of bridge cables with ice accretion at low flow turbulence. Wind and structures. Int. J. 22, 253–272. https://doi.org/10.12989/was.2016.22.2.253.

Gupta, S., Wipf, T.J., Fanous, F., Baenziger, M., Hahm, Y.H., 1994. Structural failure analysis of 345 kV transmission line. IEEE Trans. Power Deliv. 9, 894–903. https://doi.org/10.1109/61.296272.

Hrabovský, J., Gogola, R., Murín, J., Sedlár, T., 2017. Modeling of ice-shedding from ACSR power line. Strojnícky Casopis – J. Mech. Eng. 67, 45–54. https://doi.org/10.1515/scjme-2017-0005.

Ji, K., Rui, X., Li, L., Leblond, A., McClure, G., 2015. A novel ice-shedding model for overhead power line conductors with the consideration of adhesive/cohesive forces. Comput. Struct. 157, 153–164. https://doi.org/10.1016/j.compstruc.2015.05.014.

Koss, H.H., Gjelstrup, H., Georgakis, C.T., 2012. Experimental study of ice accretion on circular cylinders at moderate low temperatures. J. Wind Eng. Ind. Aerodyn. 104–106, 540–546. https://doi.org/10.1016/J.JWEIA.2012.03.024.

Lee, S., Broeren, A.P., Addy, H.E., Sills, R., Pifer, E.M., 2012. Development of 3-D ice accretion measurement method. In: Atmospheric and Space Environments Conference, pp. 1–26. https://doi.org/10.2514/6.2012–2938.

Li, J., Du, B., Su, J., Liang, H., Liu, Y., 2018. Surface layer fluorination-modulated space charge behaviors in HVDC cable accessory. Polymers 10, 500. https://doi.org/10.3390/polym10050500.

Li, L., Liu, Y., Zhang, Z., Hu, H., 2019. Effects of thermal conductivity of airframe substrate on the dynamic ice accretion process pertinent to UAS inflight icing phenomena. Int. J. Heat Mass Transf. 131, 1184–1195. https://doi.org/10.1016/J.IJHEATMASSTRANSFER.2018.11.132.

Liu, Y., Hu, H., 2018. An experimental investigation on the unsteady heat transfer process over an ice accreting airfoil surface. Int. J. Heat Mass Transf. 122, 707–718. https://doi.org/10.1016/j.ijheatmasstransfer.2018.02.023.

Liu, Y., Waldman, R., Hu, H., 2015. An experimental investigation on the unsteady heat transfer process over an ice accreting NACA 0012 airfoil. In: 53rd AIAA Aerospace Sciences Meeting, pp. 1–16. https://doi.org/10.2514/6.2015–0035.

Liu, Y., Bond, L.J., Hu, H., 2017. Ultrasonic-attenuation-based technique for ice characterization pertinent to aircraft icing phenomena. AIAA J. 55. https://doi.org/10.2514/1.J055500.

Liu, Y., Li, L., Li, H., Hu, H., 2018. An experimental study of surface wettability effects on dynamic ice accretion process over an UAS propeller model. Aerosp. Sci. Technol. 73, 164–172. https://doi.org/10.1016/J.AST.2017.12.003.

Liu, Y., Chen, W., Peng, Y., Hu, H., 2019. An experimental study on the dynamic ice accretion processes on bridge cables with different surface modifications. J. Wind Eng. Ind. Aerodyn. 190, 218–229. https://doi.org/10.1016/j.jweia.2019.05.007.

Makkonen, L., 1998. Modeling power line icing in freezing precipitation. Atmos. Res. 46, 131–142. https://doi.org/10.1016/S0169-8095(97)00056-2.

Makkonen, L., Wichura, B., 2010. Simulating wet snow loads on power line cables by a simple model. Cold Reg. Sci. Technol. 61, 73–81. https://doi.org/10.1016/J.COLDREGIONS.2010.01.008.

Meng, X., Hou, L., Wang, L., MacAlpine, M., Fu, G., Sun, B., Guan, Z., Hu, W., Chen, Y., 2012. Oscillation of conductors following ice-shedding on UHV transmission lines. Mech. Syst. Signal Process. 30, 393–406. https://doi.org/10.1016/J.YMSSP.2011.10.020.

Mulherin, N.D., 1998. Atmospheric icing and communication tower failure in the United States. Cold Reg. Sci. Technol. 27, 91–104. https://doi.org/10.1016/S0165-232X(97)00025-6.

Pohlman, J.C., Landers, P., 1982. Present state of the art of transmission line icing. IEEE Trans. Power Appar. Syst. PAS-1, 2443–2450.

Pourbagian, M., Habashi, W.G., 2013. Surrogate-based optimization of electrothermal wing anti-icing systems. J. Aircr. 50, 1555–1563. https://doi.org/10.2514/1.C032072.

Qing, H., Jian, Z., Mengyan, D., Dongmei, D., Makkonen, L., Tiihonen, M., 2019. Rime icing on bundled conductors. Cold Reg. Sci. Technol. 158, 230–236. https://doi.org/10.1016/J.COLDREGIONS.2018.08.027.

Schlichting, H., Gersten, K., Gersten, K., 2000. Boundary-Layer Theory. Springer Science & Business Media.

Szilder, K., 2018. Theoretical and experimental study of ice accretion due to freezing rain on an inclined cylinder. Cold Reg. Sci. Technol. 150, 25–34. https://doi.org/10.1016/J.COLDREGIONS.2018.02.004.

Veerakumar, R., Gao, L., Liu, Y., Hu, H., 2019. An Experimental Study of Atmospheric Icing Process on Power Transmission Line. SAE Technical Paper 2019-01-2019https://doi.org/10.4271/2019-01-2019.

Wagner, T., 2008. Atmospheric icing of transmission line conductor bundles. In: Proceedings of the COMSOL Conference 2008 Hannover.

Woodard, B.S., Broeren, A.P., Lee, S., Lum, C.W., Bragg, M.B., 2018. Summary of Ice Shape Geometric Fidelity Studies on an Iced Swept Wing. pp. 1–41. https://doi.org/10.2514/6.2018-3494.

Zarnani, A., Musilek, P., Shi, X., Ke, X., He, H., Greiner, R., 2012. Learning to predict ice accretion on electric power lines. Eng. Appl. Artif. Intell. 25, 609–617. https://doi.org/10.1016/j.engappai.2011.11.004.

Zhang, K., Wei, T., Hu, H., 2015. An experimental investigation on the surface water transport process over an airfoil by using a digital image projection technique. Exp. Fluids 56, 173. https://doi.org/10.1007/s00348-015-2046-z.